ARTICLE

Perfluoroalkyl-Functionalization of Zirconium-Based Metal–Organic Framework Nanosheets for Photosynthesis of Hydrogen Peroxide from Dioxygen and Water

Received 00th January 20xx,
Accepted 00th January 20xx

DOI: 10.1039/x0xx00000x

Yoshifumi Kondo,[a,b] Shiori Mizutani,[a] Yasutaka Kuwahara,[a,c] Kohsuke Mori,[a,c] Tohru Sekino,[b] and Hiromi Yamashita*[,a,c]

Solar-light-driven photosynthesis of hydrogen peroxide (H_2O_2) from dioxygen (O_2) and water (H_2O) is a sustainable process. Metal–organic frameworks (MOFs) are promising candidates for the photosynthesis of H_2O_2 because of their unlimited design flexibility. However, MOF-driven H_2O_2 production from O_2 and water remains a challenge because MOF photocatalysts need to exhibit high structural stability in aqueous reaction systems while suppressing H_2O_2 decomposition. In addition, the efficiency of H_2O_2 production in pure water has suffered from low O_2 solubility in aqueous solution and difficult-to-inhibit side reactions. In the present study, we demonstrate that hydrophobic Zr-based MOF nanosheets modified with perfluoroalkyl-functionalized carboxylates substantially accelerate the photocatalytic production of H_2O_2 from O_2 and H_2O under visible-light (λ > 420 nm) irradiation without any additives. Perfluoroalkyl-functionalization improves the hydrophobicity of the MOF, leading to suppression of H_2O_2 decomposition on Zr-oxo clusters. The high hydrophobicity enhances the enrichment of O_2 on the photocatalyst surface and the selectivity of two-electron oxidation of H_2O to generate H_2O_2, which promotes photocatalytic H_2O_2 synthesis. The length of the perfluoroalkyl chain plays a critical role in the enhancement of photocatalytic H_2O_2 production, and optimization of the chain length led to a 7.1-fold increase in activity compared with that of the pristine hydrophilic Zr-MOF. This study provides a noble design strategy for achieving highly selective photocatalytic H_2O_2 production via O_2 reduction and H_2O oxidation.

Introduction

Hydrogen peroxide (H_2O_2) is a crucial commodity with a wide range of industrial applications, including textile bleaching, wastewater treatment, and chemical synthesis.[1,2] Recently, H_2O_2 has also emerged as a promising liquid fuel for the compact and inexpensive one-compartment fuel cell because of its easy handling and transportability.[3,4] The annual global market for H_2O_2 reached $US 10.4 billion in 2022 and is expected to increase further to $US 15.4 billion by 2030.[5] Currently, H_2O_2 is manufactured by the anthraquinone oxidation process, which requires a high energy input and generates harmful wastes. Meeting the rapidly increasing demand for H_2O_2 necessitates the establishment of a generation method with less environmental impact. Photosynthesis is a green and sustainable approach to manufacture H_2O_2 from earth-abundant dioxygen (O_2) and water (H_2O) under solar light, as represented in eq 1:

$$O_2 + 2H_2O \rightarrow 2H_2O_2 \quad \Delta G^0 = 117\ \text{kJ·mol}^{-1} \qquad (1)$$

In the photosynthesis of H_2O_2, H_2O_2 is generated through the O_2 reduction reaction (ORR) and the H_2O oxidation reaction (WOR). In the ORR process, most recently developed photocatalysts produce H_2O_2 via the indirect two-electron ORR (2e-ORR) pathway (eqs 2 and 3) through a superoxide radical ($O_2^{\bullet-}$) intermediate:[6]

$$O_2 + e^- \rightarrow O_2^{\cdot-} \qquad (2)$$

$$2O_2^{\cdot-} + 2H^+ \rightarrow H_2O_2 \qquad (3)$$

The efficiency of H_2O_2 production via the direct 2e-ORR pathway (eq 4) is lower than that via the direct 2e-ORR pathway because of the low efficiency of the disproportionation process of superoxide radicals to form H_2O_2.[1,7,8]

$$O_2 + 2H^+ + 2e^- \rightarrow H_2O_2 \qquad (4)$$

Similarly, in the WOR pathway, the selectivity of the two-electron H_2O oxidation reaction (2e-WOR) to produce H_2O_2 should be higher than the four-electron H_2O oxidation reaction (4e-WOR) to evolve O_2. The integrated dual-channel pathway, which generates H_2O_2 via the combination of the 2e-ORR and 2e-WOR, is an ideal pathway for H_2O_2 production from O_2 and H_2O over a photocatalyst. The efficiency of atom utilization in this pathway is 100% given that O_2 and H_2O are fully utilized to produce H_2O_2 in photocatalysis. Thus, improving the efficiency of photocatalytic H_2O_2 production while maintaining the high selectivity of the 2e-ORR and 2e-WOR remains a great challenge. Suppressing the decomposition of H_2O_2 on the surface of photocatalysts is also important. Therefore, the reactivity of H_2O_2 toward metal oxides should be controlled by manipulating

[a] Division of Materials and Manufacturing Science, Graduate School of Engineering, Osaka University, 2-1 Yamadaoka, Suita, Osaka 565-0871, Japan.
[b] SANKEN, Osaka University, 8-1 Mihogaoka, Ibaraki, Osaka 567-0047, Japan.
[c] Innovative Catalysis Science Division, Institute for Open and Transdisciplinary Research Initiatives (OTRI), Osaka University, 2-1 Yamadaoka, Suita, Osaka 565-0871, Japan.

† Electronic Supplementary Information (ESI) available. See DOI: 10.1039/x0xx00000x

the catalyst structure/surface. In addition, the low solubility and low diffusion rate of O_2 in aqueous solutions have been noted as major factors restricting high-performance photocatalytic H_2O_2 production.[9,10] Numerically, the solubility of O_2 in water is quite low (8.26 mg·L^{-1} at 1 atm and 25 °C). The mass transfer limitations must be overcome to increase the O_2 concentration on the surface of photocatalysts in an aqueous reaction system.[1,11,12]

Metal–organic frameworks (MOFs) are a promising platform for photocatalysts for H_2O_2 production.[1,6,13] MOFs are a class of periodic coordination compounds composed of inorganic ions or clusters and organic linkers. MOFs are ideally suited for precisely controlling photocatalytic performance through progressive functionalization.[1,8,14,15] The combination of metal-oxo clusters and organic linkers is critical for the photosynthesis of H_2O_2 in aqueous solution. Among MOF materials, Zr-based MOFs (Zr-MOFs) exhibit superior water stability.[1,16] In addition, we have previously reported that MOFs containing porphyrin-based organic linkers enable the selective 2e-ORR in photocatalytic H_2O_2 production from O_2 and H_2O.[14] For porphyrin-based Zr-MOFs, a nanosheet morphology has been reported to enhance their photocatalytic activity compared with that of nanoparticles because nanosheets enable rapid mass transport and provide a large number of exposed catalytically active sites.[17] Therefore, a porphyrin-based Zr-MOF nanosheet is a promising candidate for the photosynthesis of H_2O_2. Some of the most attractive strategies include functionalization at the metal-oxo clusters and covalent modification of the organic linkers; both of these approaches improve the photocatalytic activity by optimizing the surface adsorption and light absorption abilities of MOFs. In particular, ligand engineering of MOF catalysts enables control of their hydrophobicity/hydrophilicity via alkyl modification of metal-oxo clusters or organic linkers.[1,6,18] We previously found that hydrophobic acetate ligands coordinated at metal-oxo clusters can inhibit H_2O_2 decomposition on metal-oxo clusters in MOFs.[12,16] Acetate ligands at the cluster defects reduce the reactivity of H_2O_2 with the clusters and promote the diffusion of H_2O_2 to the exterior of MOFs by improving the inner-surface hydrophobicity of MOFs, resulting in suppression of H_2O_2 decomposition.

Based on the above considerations, we herein focus on the interaction between the hydrophobic/hydrophilic surface of photocatalysts and polar/nonpolar substrates/products (O_2, H_2O, and H_2O_2) as a critical factor controlling the photocatalytic activity (**Scheme 1**). Hydrophobic surfaces allow more gas-phase O_2 molecules to reach reaction sites, substantially increasing the surface concentration of O_2 and promoting O_2 reduction. Furthermore, polar H_2O_2 molecules are expected to easily desorb from the surface of photocatalysts if the surface is hydrophobic.[9,10,19,20] The rapid desorption of H_2O_2 suppresses its decomposition and enhances the 2e-WOR because H_2O_2 is an intermediate of the 4e-WOR to produce O_2 from H_2O.[21–23] Therefore, constructing a hydrophobic interface is expected to be a feasible and effective strategy to overcome the mass transfer limitations of O_2 in aqueous solutions, increase the selectivity of the 2e-WOR to produce H_2O_2, and suppress H_2O_2 decomposition (**Scheme 1**).[9]

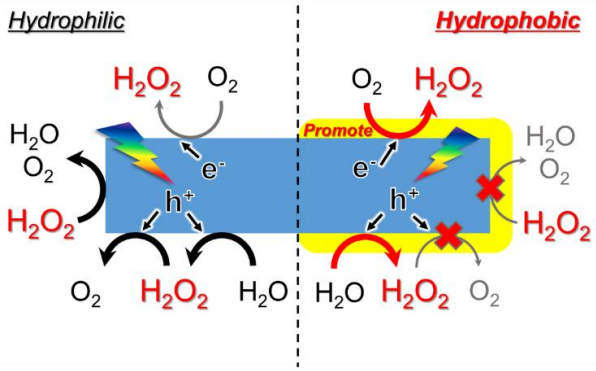

Scheme 1 Strategy for the hydrophobization of photocatalysts to accelerate H_2O_2 production.

In the present study, to enhance photocatalytic activity for H_2O_2 production, we used perfluoro-functionalization of porphyrin-based Zr-MOF nanosheets (Zr-TCPP, where TCPP = tetrakis(4-carboxyphenyl)porphyrin) to control the adsorption of O_2 and H_2O_2 onto the surface of the Zr-MOF photocatalyst. We tuned the degree of hydrophobicity by modifying Zr-TCPP with perfluorocarboxylates with alkyl groups of different lengths. The perfluoro-functionalization of Zr-TCPP with alkyl groups with the appropriate length provided 7.2-fold higher activity for H_2O_2 production from O_2 and H_2O in pure water under visible-light irradiation when compared with the activity of pristine Zr-TCPP. The hydrophobicity provided by perfluoro-functionalization facilitates the adsorption of O_2 in an aqueous solution, suppresses the decomposition of H_2O_2 on the Zr-oxo clusters, and enhances the selectivity of the 2e-WOR to produce H_2O_2 from H_2O, as evidenced by electron-spin resonance (ESR) measurements and comparative experiments.

Experimental

Materials

TCPP, nonafluorovaleric acid, tridecafluoroheptanoic acid, nonadecafluorodecanoic acid, tricosafluorododecanoic acid, 5,5-dimethyl-1-pyrroline *N*-oxide (DMPO), 2,2,6,6-tetramethylpiperidine (TEMP), *p*-benzoquinone (*p*-BQ) and oxo[5,10,15,20-tetra(4-pyridyl)porphinato]titanium(IV) ($TiO(tpypH_4)^{4+}$) were purchased from Tokyo Chemical Industry. Zirconium chloride ($ZrCl_4$), *N*,*N*-dimethylformamide (DMF), formic acid (HCOOH), acetone, acetonitrile, decanoic acid, H_2O_2, hydrochloric acid (HCl), perchloric acid ($HClO_4$), methanol, sodium azide (NaN_3), and potassium bromate ($KBrO_3$) were purchased from Nacalai Tesque. Sulfuric acid-d_2 (D_2SO_4) and dimethyl sulfoxide-d_6 (DMSO-d_6) were obtained from Sigma-Aldrich. All chemicals were used as received without further purification.

Synthesis of Zr-TCPP

Zr-TCPP was prepared according to a previously reported method, with some modifications (Scheme 2a).[17] $ZrCl_4$ (1.12 g) was dissolved

in DMF (120 mL). Then, TCPP (0.63 g), distilled water (52.8 mL), and formic acid (60 mL) were added to the solution. The obtained solution was transferred to a 40 mL Teflon liner in a stainless-steel autoclave and heated at 120 °C for 3 days. The obtained purple solid was centrifuged and washed with DMF, distilled water, and acetone several times.

Synthesis of perfluoroalkene-functionalized Zr-TCPP (Zr-TCPP-RF*x*; *x* = 4, 6, 9, 11)

Zr-TCPP (0.20 g) was added to an acetonitrile solution (200 mL) containing various perfluorocarboxylic acids (2.5 mmol·L^{-1}) (Scheme 2b). **Table S1** summarizes the perfluorocarboxylic acids used in the present study. The solution was stirred at 60 °C for 1 h. The obtained solid was collected by centrifugation, washed with acetonitrile several times, and dried under vacuum overnight. The corresponding product was denoted as Zr-TCPP-RF*x*, where *x* denotes the carbon number of a modified $C_xF_{2x+1}COOH$ agent.

Results and discussion

Characterizations of Zr-TCPP modified with various perfluoroalkyl carboxylic acids (Zr-TCPP-RF*x*)

Zr-TCPP was synthesized using a solvothermal method with a high concentration of formic acid in DMF solution at 120 °C for 3 days.[17,24] Perfluoroalkylation of Zr-TCPP was conducted by mixing with an acetonitrile solution containing a perfluoroalkyl carboxylic acid at 60 °C for 1 h (Scheme 2a).[18,24] The series of perfluoroalkylated Zr-TCPP was named Zr-TCPP-RF*x*, where *x* represents the carbon number of the perfluorinated group ($C_xF_{2x+1}COOH$) (Scheme 2b).

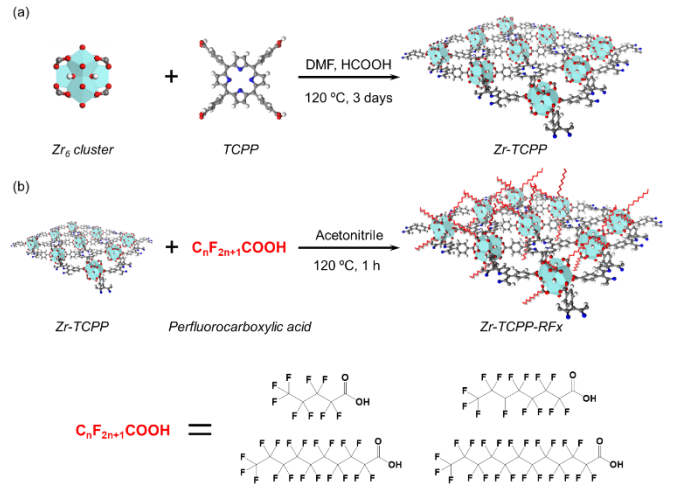

Scheme 2 Schematic of the preparation of (a) Zr-TCPP and (b) Zr-TCPP-RF*x*.

The modification of perfluoroalkyl carboxylates on Zr-TCPP was confirmed by Fourier transform infrared (FT-IR) spectroscopy. The FT-IR spectra of Zr-TCPP-RF*x* (**Fig. 1a**) confirmed the appearance of an intense doublet signal at 1170 and 1205 cm^{-1}, originating from the symmetric and antisymmetric C–F stretching vibrations, respectively.[25–27] The intensity of these signals was strengthened by lengthening perfluoroalkyl chains modified on Zr-TCPP-RF*x*. Elemental analysis of Zr-TCPP-RF*x* was performed using energy-dispersive X-ray spectrometry (EDS). **Table 1** summarizes the fluorine (F) content of Zr-TCPP-RF*x*. The F content in Zr-TCPP-RF*x* increased with increasing chain length of the perfluoroalkyl functional groups. The amount of perfluorocarboxylic acid modified on the Zr-oxo cluster was calculated from the Zr/F molar ratio. Each Zr-oxo cluster was modified with approximately 4.5–5 perfluorocarboxylates. The number of perfluorocarboxylates per Zr-oxo cluster coordinated on Zr-TCPP-RF*x* did not substantially differ.

Proton nuclear magnetic resonance (^{1}H-NMR) spectroscopy was performed to investigate the pathway by which perfluorocarboxylic acid modifies Zr-TCPP. In the ^{1}H-NMR spectra of Zr-TCPP, the peak derived from the C–H bond of formate was observed at 8.0 ppm (**Fig. S1**). Formic acid acts as a mediator for constructing the nanosheet morphology by occupying the coordination sites to weaken the interaction of interlayers.[17] The peak at 8.0 ppm disappeared after perfluoro-functionalization. These results demonstrate that perfluorocarboxylates were coordinated on the Zr-oxo clusters via ligand-exchange reaction from formate ligands or via modification at Zr-bound hydroxyl groups.[18,24]

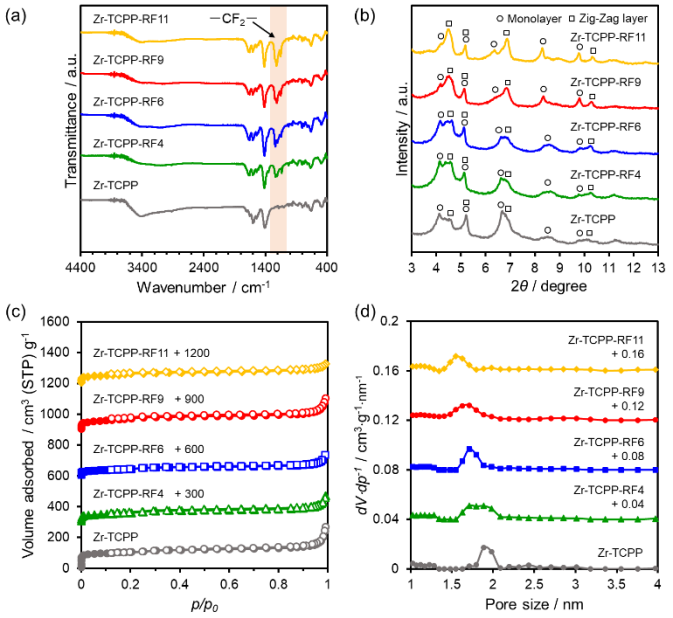

Fig. 1 (a) FT-IR spectra, (b) XRD patterns, (c) N_2 adsorption–desorption isotherms, and (d) pore distributions calculated by the NLDFT method for Zr-TCPP and Zr-TCPP-RF*x*.

Table 1 EDS elemental analysis of Zr-TCPP-RF*x*.

Sample	F (wt%)	Zr (wt%)	Coordination number per Zr-oxo cluster
Zr-TCPP-RF4	17.5	11.0	5.09
Zr-TCPP-RF6	23.6	10.9	4.80
Zr-TCPP-RF9	29.0	8.9	4.94
Zr-TCPP-RF11	31.7	8.7	4.56

Powder X-ray diffraction (XRD) measurements were performed to identify the crystal structures of Zr-TCPP and Zr-TCPP-RF*x* (**Fig. 1b**). The XRD pattern of Zr-TCPP was consistent with previous reports.[17,24]

According to Wang et al., the XRD pattern indicates a monolayer and zig-zag layer crystal structure of TCPP-based Zr-MOF nanosheets.[24] Zr-TCPP is composed of two different crystal structures: a monolayer and a zigzag layer. Perfluorocarboxylic acid modification decreased the intensity of the main peaks of the monolayer structure at ~4.2° and ~6.7°, and increased the intensity of the main peaks of the zig-zag structure at ~4.6° and ~6.9°.[24] Therefore, the crystal structure of Zr-TCPP-RF*x* was estimated to change from a monolayer to a zig-zag layer with increasing length of the alkyl chains of the perfluorocarboxylic acid.

The porous structure and surface area were investigated using N_2 adsorption–desorption measurements. Zr-TCPP and Zr-TCPP-RF*x* exhibited a type-I isotherm (**Fig. 1c**), indicating that they are microporous materials. **Table 2** summarizes the Brunauer–Emmett–Teller (BET) surface area (S_{BET}) and total pore volume (V_{total}) of Zr-TCPP and Zr-TCPP-RF*x*. The S_{BET} and V_{total} values of Zr-TCPP-RF*x* are smaller than those of the pristine Zr-TCPP. **Fig. 1d** displays the pore size distributions of Zr-TCPP and Zr-TCPP-RF*x*, as calculated using the non-local density functional theory (NLDFT) method. Zr-TCPP and Zr-TCPP-RF*x* contain ~2.0 nm micropores. Modification with longer-chain perfluoroalkyl carboxylic acids resulted in a smaller 2.0 nm pore. The ~2.0 nm pore size matches the distance between two adjacent secondary Zr-oxo nodes in the crystal model (1.7143 Å).[17] Perfluorocarboxylates modify the Zr-oxo clusters, plugging the pores and reducing the pore size. Thus, the perfluoro-modification reduced the S_{BET} and V_{total} values of the MOFs because of the occupation of the pore spaces.

Table 2 The molar ratio of the TCPP and TBAPy linkers in the Al-TCPP(10-X)-TBAPyX samples.

Sample	S_{BET}[a] ($m^2 \cdot g^{-1}$)	V_p[b] ($cm^3 \cdot g^{-1}$)
Zr-TCPP	389	0.38
Zr-TCPP-RF4	210	0.25
Zr-TCPP-RF6	152	0.21
Zr-TCPP-RF9	258	0.31
Zr-TCPP-RF11	214	0.19

[a] Determined the BET method by N_2 adsorption data using ISO 9227 standard.
[b] Total pore volume reported at p/p_0 = 0.99.

Transmission electron microscopy (TEM) and field-emission scanning electron microscopy (FE-SEM) were used to observe the morphologies of Zr-TCPP and Zr-TCPP-RF9. The TEM images show uniform thin sheets in both Zr-TCPP and Zr-TCPP-RF9 (**Fig. S2**). FE-SEM images further confirm that Zr-TCPP and Zr-TCPP-RF9 exhibit a nanosheet morphology with a thickness of ~7.6 nm. The thickness corresponds to a sheet of 4-5 layers.[17,24] Elemental mapping using energy-dispersive X-ray spectroscopy (EDX) revealed that C, N, O, and Zr were overlapped in the Zr-TCPP nanosheet (**Fig. 2a**). In addition, F was detected and observed to be well-dispersed in the Zr-TCPP-RF9 nanosheet (**Fig. 2b**). These results demonstrate that perfluoro-functionalization was uniform on Zr-TCPP-RF*x* and that the morphology of the photocatalysts was not changed by the perfluoro-functionalization.

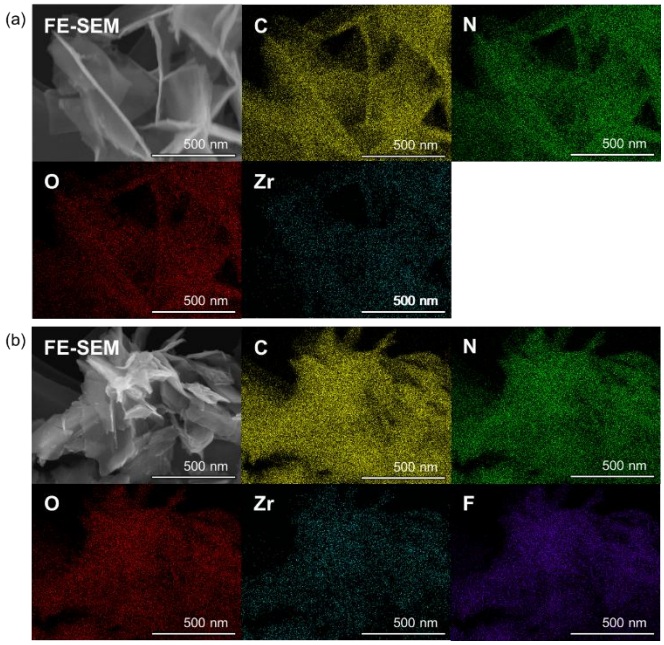

Fig. 2. FE-SEM images and EDX elemental mappings of (a) Zr-TCPP and (b) Zr-TCPP-RF9.

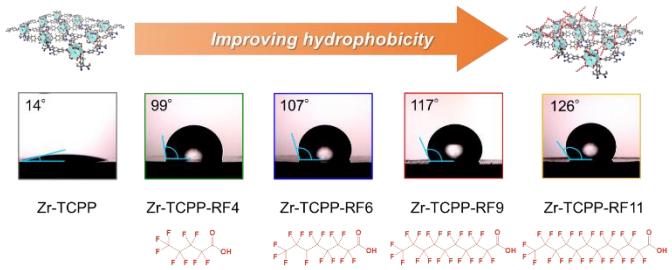

Fig. 3 The contact angles of water droplets on Zr-TCPP and Zr-TCPP-RF*x*.

The hydrophobicity/hydrophilicity of Zr-TCPP and Zr-TCPP-RF*x* were evaluated by water contact angle measurements.[6,25] The contact angle of a water droplet on the pristine Zr-TCPP was 14°, indicating that its surface is hydrophilic (**Fig. 3**). Although perfluoroalkyl-functionalized Zr-TCPP-RF*x* had contact angles greater than 90°, longer alkyl chains of the perfluorocarboxylic acids used to modify Zr-TCPP-RF*x* increased the water contact angles of Zr-TCPP-RF*x* (**Fig. 3**). These results show that the perfluoro-functionalization changed the surface of Zr-TCPP from hydrophilic to hydrophobic.

Fig. 4a shows diffuse-reflectance UV–Vis spectra of Zr-TCPP and Zr-TCPP-RF*x*. The spectrum of Zr-TCPP shows a strong Soret band at 380 nm and four Q-band peaks in the wavelength range 450–700 nm.[28] The four Q-band peaks indicate that no metal species were inserted into the porphyrin rings.[29] Irrespective of the perfluoro-functionalization, no substantial differences were observed in the Q-bands between Zr-TCPP and Zr-TCPP-RF*x*. By contrast, in the Zr-TCPP-RF*x* series, the peak intensity of the Soret band increased and the peak shifted to the longer-wavelength side compared with the corresponding peak in the spectrum of bare Zr-TCPP. As shown in **Fig. 4b**, the length of the alkyl group of the perfluorocarboxylic acid used to modify Zr-TCPP-RF*x* is positively correlated with an increase in peak intensity and a red-shift of the Soret band from 374 to 388 nm. The absorption of Soret band is known to vary with the electrical interactions and the arrangement of the porphyrin rings.[30–33]

X-ray photoelectron spectroscopy (XPS) measurements were performed to evaluate the electronic state of Zr in Zr-TCPP and Zr-TCPP-RF*x*. **Fig. 4c** presents the Zr 3d XPS spectra of the photocatalysts. The binding energy of Zr $3d_{5/2}$ gradually shifted to the high-energy side with increasing chain length of the perfluorocarboxylates used to modify Zr-TCPP-RF*x*. These results indicate that Zr species become more electron-deficient with increasing length of the perfluoroalkyl chains modifying Zr-TCPP-RF*x* (**Fig. 4d**). In addition, the MOF crystal structures also affect the charge state of metal-oxo clusters.[8] As shown in **Fig. 1b**, perfluoro-functionalization gradually changes the crystal structure of Zr-TCPP-RF*x*. Therefore, the change of the Zr species to the electron-deficient state is presumably due to the electron-withdrawing ability of the perfluorocarboxylates and the change in the crystal structure of the Zr-MOFs.

The electron-deficient Zr species in clusters exhibit strong electron-withdrawing ability toward the TCPP linkers. The Soret band has been reported to red-shift upon introduction of an electron-withdrawing group into the porphyrin ring.[30] Therefore, we infer that a similar electron-withdrawing effect may occur on the electron-deficient Zr cluster, resulting in red-shifts of the Soret band. The Soret band is also sensitive to the arrangement of the porphyrin rings, such as porphyrin aggregates.[31–33] The crystal structures of Zr-MOFs change when the length of the alkyl group of the perfluorocarboxylates is varied (**Fig. 1b**). Similar to porphyrin aggregates, the change in the crystal structure of the Zr-MOFs may also be responsible for the increase in peak intensity and red-shift of the Soret band.

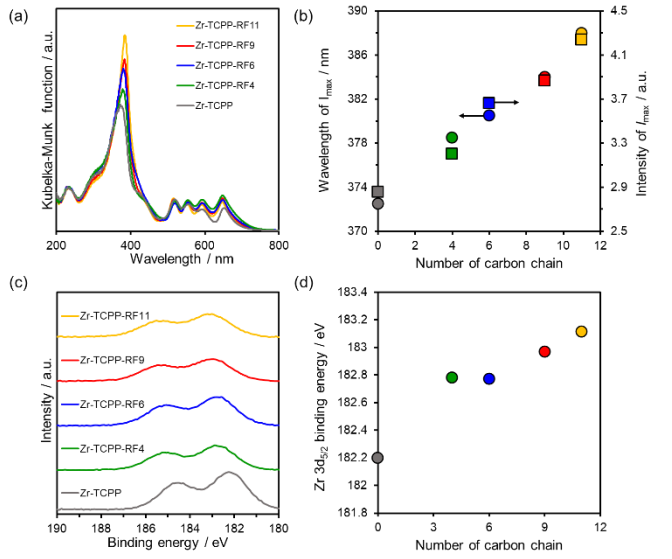

Fig. 4 (a) Diffuse-reflectance UV–Vis spectra of Zr-TCPP and Zr-TCPP-RF*x*. (b) Relationship between wavelength or maximum peak intensity (I_{max}) in the UV–Vis spectra and the carbon number of the perfluorocarboxylate chain modifying Zr-TCPP-RF*x*. (c) Zr 3d XPS spectra of Zr-TCPP and Zr-TCPP-RF*x*. (d) Relationship between the Zr $3d_{5/2}$ binding energy and the carbon number of the perfluorocarboxylate chain modifying Zr-TCPP-RF*x*.

Photosynthesis of H_2O_2 from O_2 and H_2O using Zr-TCPP-R*Fx*

The photocatalytic performance of Zr-TCPP-RF*x* toward H_2O_2 production was evaluated in O_2-saturated distilled water under visible-light ($\lambda > 420$ nm, 100 mW·cm^{-2}) irradiation. As-obtained MOF photocatalysts continuously produced H_2O_2 under visible-light irradiation (**Fig. S3**). **Fig. 5a** shows the H_2O_2 production rates for Zr-TCPP and Zr-TCPP-RF*x*. The H_2O_2 yield was enhanced by the modification of Zr-TCPP with perfluorocarboxylates. In particular, Zr-TCPP-RF9 exhibited the highest H_2O_2 yield, which was 7.2 times higher than the yield obtained with bare Zr-TCPP. Zr-TCPP-RF9 showed superior photocatalytic activity compared to previously reported MOF photocatalysts (**Table S2**). However, a marked decrease in photocatalytic performance was observed for Zr-TCPP-RF11. These results demonstrate that the H_2O_2 yield is maximized by hydrophobization using the perfluorocarboxylic acid with the optimal alkyl chain length.

To gain insights into the mechanism of photocatalytic H_2O_2 production using Zr-TCPP-RF9, we conducted control experiments. As shown in **Fig. 5b**, no H_2O_2 was detected in the absence of O_2, H_2O, and visible light. These results reveal that H_2O_2 was photocatalytically produced from O_2 and H_2O by Zr-TCPP-RF9.

Fig. 5c shows the results of recycling tests using Zr-TCPP-RF9. The Zr-TCPP-RF9 could be recycled at least three times while maintaining its original activity. XRD patterns showed that its crystal structure and crystallinity were retained after the recycling tests, indicating that Zr-TCPP-RF9 exhibits high reusability and stability (**Fig. S4**).

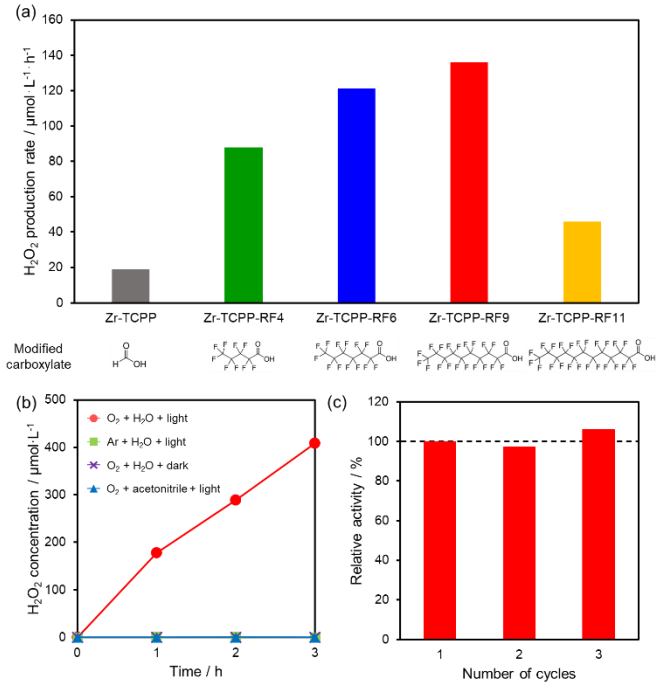

Fig. 5 (a) Comparison of photocatalytic H_2O_2 production over Zr-TCPP and Zr-TCPP-RF*x* in O_2-saturated distilled water under visible-light ($\lambda > 420$ nm) irradiation. (b) Comparison of photocatalytic H_2O_2 production over Zr-TCPP-RF9 under various conditions. (c) Recycle tests for H_2O_2 production with Zr-TCPP-RF9.

Effect of perfluoroalkyl chains of carboxylates modified on Zr-TCPP and MOF morphology on H_2O_2 production

To investigate the effect of fluorination of alkyl chains, Zr-TCPP-RH9 was prepared by modifying Zr-TCPP with decanoic acid. No substantial differences were observed in the original crystal structure and the crystallinity of Zr-TCPP after the decanoic acid modification

(**Fig. S5a**). The presence of decanoic acid on Zr-TCPP-RH9 was confirmed by the appearance of two peaks (2920 and 2850 cm^{-1}) assigned to the symmetric and asymmetric stretching vibration of C–H in the alkyl groups of decanoic acid, respectively, in the FT-IR spectrum (**Fig. S5b**). The water contact angle for Zr-TCPP-RH9 was 53°, exceeding 30°, indicating that Zr-TCPP-RH9 is hydrophobic (**Fig. S5c**).

Fig. 6a illustrates photocatalytic H_2O_2 production using Zr-TCPP-RH9 under visible-light (λ > 420 nm) irradiation. Compared with the H_2O_2 production of pristine Zr-TCPP, that of the hydrophobic material modified using decanoic acid (i.e., Zr-TCPP-RH9) was enhanced. However, the activity enhancement of Zr-TCPP-RH9 was smaller than that of perfluorodecanoic acid-modified Zr-TCPP-RF9. Based on the water contact angle of Zr-TCPP-RF9 and Zr-TCPP-RH9 (**Fig. 3 and Fig. S5c**), decanoic acid-modification may impart insufficient hydrophobicity to Zr-TCPP-RH9 compared to Zr-TCPP-RF9. This result indicates that fluorination of the carboxylic acid used to modify Zr-TCPP accelerates photocatalytic H_2O_2 production.

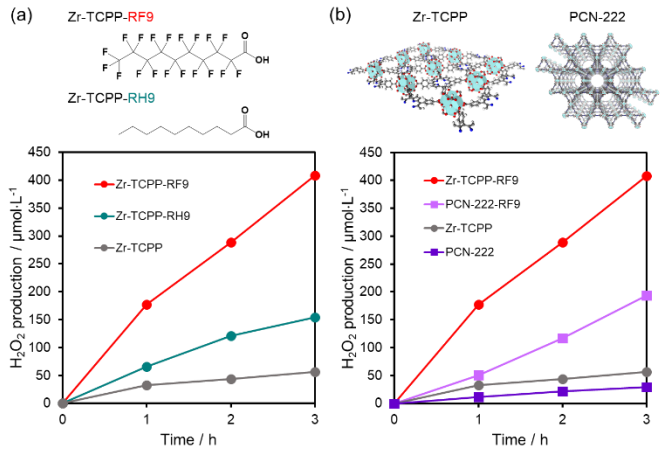

Fig. 6 (a) Comparison of photocatalytic H_2O_2 production performance over Zr-TCPP, Zr-TCPP-RF9, and Zr-TCPP-RH9. (b) Effect of morphology on the photocatalytic production of H_2O_2 under visible-light (λ > 420 nm) irradiation.

The nanosheet-like structure of as-synthesized Zr-TCPP was constructed by replacing part of three-dimensional-coordinated TCPP linkers with formic acid by adding a high concentration of formic acid during the synthesis.[17] To clarify the effect of the MOF morphology on photocatalysis, we synthesized a similar analog with a different morphology: porphyrin-based Zr-MOF (PCN-222) nanoparticles and PCN-222 nanoparticles hydrophobically modified using perfluorodecanoic acid (PCN-222-RF9). PCN-222 and PCN-222-RF9 are composed of rice-ball-like nanoparticles with a particle size of ~200 nm (**Fig. S6a,b**). The modification of PCN-222 with perfluorodecanoic acid did not substantially affect its crystal structure or morphology, although it slightly reduced its crystallinity (**Fig. S6a–c**).

PCN-222-RF9 also exhibited hydrophobicity after being modified with perfluorodecanoic acid (**Fig. S6d**). **Fig. 7b** shows H_2O_2 production using PCN-222 and PCN-222-RF9. Hydrophobic PCN-222-RF9 showed 6.5-fold greater photocatalytic activity than the pristine hydrophilic PCN-222. However, compared with Zr-TCPP-RF9, PCN-222-RF9 produced less H_2O_2 and showed a lower activity enhancement by hydrophobization. In addition, Zr-TCPP exhibited greater photocatalytic activity than PCN-222. Compared with PCN-222 nanoparticles, ultrathin Zr-TCPP nanosheets offer substantial advantages, presumably because of several positive factors such as facile mass transfer and abundant accessible active sites on their surface.[17,34] After the perfluoro-functionalization, the hydrophobic groups on the modified particle surface may inhibit the diffusion of H_2O into the Zr-MOF pore interior.[35,36] Therefore, the number of photocatalytic sites that can act as a H_2O oxidation center is limited in PCN-222 nanoparticles with a three-dimensional structure, resulting in a lower activity enhancement by hydrophobization compared with the enhancement observed for Zr-TCPP nanosheets. Thus, Zr-TCPP nanosheets are a promising platform for promoting H_2O_2 production through modification using perfluorocarboxylates.

Effect of hydrophobicity on H_2O_2 decomposition

The suppression of H_2O_2 decomposition plays a critical role in improving the yield of H_2O_2.[1] **Fig. 7a** shows a comparison of the H_2O_2 decomposition rates of Zr-TCPP and Zr-TCPP-RF*x* in the dark. H_2O_2 decomposition was inhibited by lengthening the alkyl chain of the perfluorocarboxylates used to modify Zr-TCPP-RF*x*. The hydrophobicity increased with increasing alkyl chain length of the perfluorocarboxylates used to modify Zr-TCPP-RF*x* (**Fig. 3**). Some hydrophobic photocatalysts have been reported to be spatially separated from H_2O_2, thus avoiding H_2O_2 decomposition and contributing to the accumulation of a high-concentration H_2O_2 solution.[1,6,9] In addition, H_2O_2 decomposition by MOFs is known to proceed via the disproportionation of H_2O_2 (eq 5):[7]

$$2H_2O_2 \rightarrow 2H_2O + O_2 \quad (5)$$

The disproportionation of H_2O_2 is promoted by the formation of Zr-OOH species at Zr-oxo clusters of Zr-MOFs.[16] Previous studies have demonstrated that modification of Zr-oxo clusters with hydrophobic acetate ligands increases the activation energy for the formation of Zr-OOH species and effectively separates the produced H_2O_2 from the MOF photocatalyst because of its hydrophobicity, resulting in suppression of the decomposition of H_2O_2.[12,16] Therefore, the suppression of H_2O_2 decomposition is presumably due to the diminished reactivity between H_2O_2 and Zr-oxo clusters as a result of the surface being rendered superhydrophobic through the cluster modification using perfluorocarboxylates. Notably, with Zr-TCPP-RF11, the initial concentration of H_2O_2 was maintained for 4 h (**Fig. S7**), indicating that the superhydrophobicity of Zr-TCPP-RF11 prevents the decomposition of H_2O_2 by providing good separation between H_2O_2 and Zr-oxo clusters. This excessively strong hydrophobicity can prevent the absorption of not only H_2O_2 but also H_2O, which is necessary for the H_2O oxidation process that consumes photogenerated holes, leading to a low yield of H_2O_2. Other studies have reported that excessive hydrophobicity inhibits the reactivity of photocatalysts with H_2O.[10,37] We infer that H_2O_2 production catalyzed by Zr-TCPP-RF11 underperformed H_2O_2 production catalyzed by Zr-TCPP-RF9 because of this excessively strong hydrophobicity (**Fig. 5a**).

Reaction pathway for H_2O_2 production over Zr-TCPP-RF*x*

ESR measurements were performed to confirm the active oxygen species involved in the reaction using Zr-TCPP and Zr-TCPP-RF9. DMPO was used as a radical trapping agent to identify superoxide

radicals ($O_2^{\bullet-}$) and hydroxyl radicals (•OH).[38] Neither Zr-TCPP nor Zr-TCPP-RF9 produced DMPO–$O_2^{\bullet-}$ signals with or without visible-light irradiation (**Fig. 7b**). Radical trapping tests with *p*-benzoquinone (*p*-BQ) for $O_2^{\bullet-}$ and *tert*-butyl alcohol (*t*-BA) for •OH also showed no contribution of $O_2^{\bullet-}$ and •OH to H_2O_2 production (**Fig. S8**). These results show that the H_2O_2 production pathway of Zr-TCPP and Zr-TCPP-RF9 is not the indirect 2e-ORR (eqs 2 and 3) but the direct 2e-ORR (eq 4).[14]

MOFs containing porphyrin-based linkers generate singlet oxygen ($^1O_2$) via excited energy transfer to O_2.[14] ESR measurements using TEMP were conducted to confirm the generation of $^1O_2$ species during the reactions using Zr-TCPP and Zr-TCPP-RF9. Under visible-light irradiation, a clear triplet signal was observed when TEMP and one of the photocatalysts were both present. The signal was identified as being associated with 2,2,6,6-tetramethylpiperidine 1-oxyl (TEMPO), indicating that Zr-TCPP and Zr-TCPP-RF9 produce $^1O_2$ via a light-induced energy transfer process (eq 6) (**Fig. 7c**). Such $^1O_2$ intermediates are known to facilitate the direct 2e-ORR (eq 7), which is consistent with the results of ESR measurements using DMPO.[14,39] In addition, the TEMPO signal of Zr-TCPP-RF9 was substantially stronger than that of Zr-TCPP, manifesting that Zr-TCPP-RF9 promotes O_2 activation as a result of its hydrophobicity. Based on the results of O_2-bubble contact angles (Fig. 7d), the hydrophobization of Zr-TCPP using perfluoroalkyl groups increased its affinity toward O_2. In order to clarify the effect of hydrophobization on energy and electron transfer from the excited Zr-MOFs to O_2, photoluminescence (PL) measurements were performed under Ar and O_2 atmosphere. **Fig. S9** shows the quenching efficiency (QE = (1-I_{O2}/I_{Ar}) × 100%) of the PL spectra by O_2. The quenching of PL intensity was larger for Zr-TCPP-RF9 (22%) than for Zr-TCPP (14%). These results indicate that hydrophobization via perfluoro-functionalization improves the affinity of O_2, resulting in accelerating the energy transfer to generate $^1O_2$ (eq 6) and the electron transfer in the direct 2e-ORR (eqs 7).

$$O_2 \xrightarrow{h\nu} {}^1O_2 \quad (6)$$

$$^1O_2 + 2H^+ + 2e^- \rightarrow H_2O_2 \quad (7)$$

The formation of $^1O_2$ intermediates provides another possibility for the H_2O_2 formation pathway: direct H_2O oxidation by $^1O_2$ species (eq 8).[40–42] The proposed reaction pathway to produce H_2O_2 over Zr-TCPP and Zr-TCPP-RF9 is expressed as

$$^1O_2 + 2H_2O \rightarrow 2H_2O_2 \quad (8)$$

Thus, hydrophobization of Zr-TCPP through perfluoro-functionalization improves the adsorption ability of O_2, thereby accelerating the 2e-ORR and the direct H_2O oxidation process to generate H_2O_2.[14]

The effect of perfluoro-functionalization on H_2O oxidation was also investigated. As shown in Fig. 7b, no DMPO–•OH signals were detected when Zr-TCPP and Zr-TCPP-RF9 were used under visible-light irradiation. Zr-TCPP and Zr-TCPP-RF9 were incapable of producing •OH via single-electron oxidation of H_2O (eq 9). These results discount the production pathway of H_2O_2 via disproportionation of •OH (eq 10). Therefore, the oxidation pathway of H_2O is presumably via the 2e-WOR to produce H_2O_2 (eq 11) and the 4e-WOR to generate O_2 (eq 12).

$$H_2O + h^+ \rightarrow \cdot OH + H^+ \quad (9)$$

$$2 \cdot OH \rightarrow H_2O_2 \quad (10)$$

$$2H_2O + 2h^+ \rightarrow H_2O_2 + 2H^+ \quad (11)$$

$$2H_2O + 4h^+ \rightarrow O_2 + 4H^+ \quad (12)$$

The quantification of products from H_2O oxidation using Zr-TCPP and Zr-TCPP-RF9 was assessed in a potassium bromate ($KBrO_3$) aqueous solution under Ar atmosphere and visible-light (λ > 420 nm) irradiation. $KBrO_3$ acts as an electron scavenger.[2,12] **Fig. 7e** shows the H_2O oxidation products generated during 3 h of visible-light (λ > 420 nm) irradiation, confirming the formation of O_2 and H_2O_2. Interestingly, Zr-TCPP produced mainly O_2, whereas Zr-TCPP-RF9 showed highly selective H_2O_2 production in the WOR. Perfluoro-functionalization of Zr-oxo clusters dramatically enhanced the selectivity of H_2O_2 via H_2O oxidation from 31% to 91%. H_2O_2 is known to be an intermediate in the 4e-WOR pathway.[43] The low wettability of H_2O_2 on the hydrophobic surface of Zr-TCPP-RF9 promotes the desorption of H_2O_2, preventing its over-oxidation to H_2O (**Fig. 7f**).[19,21] In addition, valence band (VB) position of photocatalysts affects the selectivity of H_2O oxidation.[1,9] **Fig. S10** shows the XPS VB spectra of Zr-TCPP and Zr-TCPP-RF9. From XPS VB Spectra, the highest occupied crystal orbital (HOCO) levels of Zr-TCPP and Zr-TCPP-RF9 were calculated to 2.70 V vs NHE and 2.69 V vs NHE, respectively. These results indicate that the electric structure is little changed before and after perfluoro-functionalization. The highest occupied crystal orbital (HOCO) levels of Zr-TCPP and Zr-TCPP-RF9 are higher than the energy level of 2e-WOR (1.76 V vs NHE) and 4e-WOR (1.23 V vs NHE) but insufficient for the energy level of 1e-WOR (2.73 V vs NHE). These results show that 1e-WOR with Zr-TCPP and Zr-TCPP-RF9 is not thermodynamically favourable, which agrees with the ESR results (**Fig. 7b**). Thus, perfluoro-functionalization is presumed to provide the positive effect on enhancing the selectivity 2e-WOR from the surface hydrophobicity not electronic structure of Zr-MOFs.

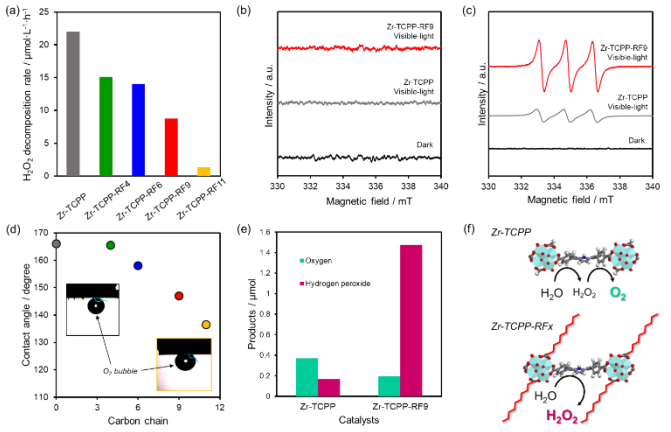

Fig. 7 (a) H_2O_2 decomposition rates of Zr-TCPP and Zr-TCPP-RF*x* in the dark. (b, c) ESR spectra demonstrating active oxygen species of Zr-TCPP and Zr-TCPP-RF9 under dark and visible-light (λ > 420 nm) irradiation conditions. (b) DMPO and (c) TEMP were used as $O_2^{\bullet-}$ and $^1O_2$ trapping agents, respectively. (d) Relationship between the contact angles of O_2 bubbles on Zr-TCPP and Zr-TCPP-RF*x* and the carbon number of the perfluorocarboxylate chain modifying Zr-TCPP-RF*x*. (e) Comparison of H_2O oxidation products over Zr-TCPP and Zr-TCPP-RF9 during 3 h of visible-light irradiation in a $KBrO_3$ aqueous solution under Ar atmosphere. (f) Schematic of H_2O oxidation on Zr-TCPP and Zr-TCPP-RF9.

Proposed reaction mechanisms for Zr-TCPP-RF9

Based on the above results, we propose the following reaction mechanisms for H_2O_2 production over Zr-TCPP-RF9 (**Scheme 3**). The

H_2O_2 production process is initiated by the photoexcitation of the TCPP linkers under visible-light irradiation. The TCPP linkers transfer to the triplet state of the excited TCPP linkers. The triplet state of the TCPP linkers relaxes and provides energy transfer toward O_2 to generate $^1O_2$. The $^1O_2$ species are two-electron reduced by photoexcited electrons of the MOFs, accompanied by a reaction with H^+ in H_2O to produce H_2O_2. By contrast, generated holes selectively produce H_2O_2 via H_2O oxidation. In addition, $^1O_2$ species can directly oxidize H_2O to generate H_2O_2. The hydrophobic surface on Zr-TCPP-RF9 prevents H_2O_2 decomposition. The hydrophobization of Zr-TCPP using perfluorocarboxylates promotes O_2 reduction, enhances the selectivity of the 2e-WOR to produce H_2O_2, and inhibits H_2O_2 decomposition, resulting in a substantially improved H_2O_2 yield.

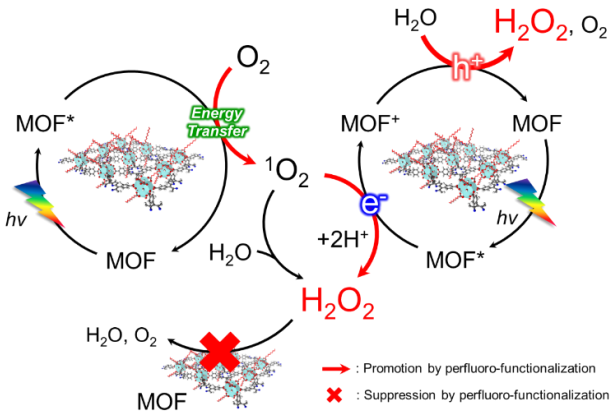

Scheme 3 Schematic of the reaction mechanism involving Zr-TCPP-RF9.

Conclusions

In conclusion, we demonstrated an effective strategy for promoting the photosynthesis of H_2O_2 using hydrophobically modified MOF photocatalysts. Perfluoro-functionalization of Zr-TCPP changed the crystal structure from monolayer to zig-zag layer. The Soret band in the absorption spectrum of Zr-TCPP-RFx was intensified and was shifted to longer wavelengths because of the change in the crystal structure of the MOFs, the associated change in the electron-withdrawing ability of perfluorocarboxylates, and the formation of electron-deficient Zr species in Zr-oxo clusters. Longer alkyl chains of the perfluorocarboxylates used to prepare Zr-TCPP-RF*x* led to greater hydrophobicity. In particular, the highest H_2O_2 production was achieved when nonafluorodecanoic acid was used to modify Zr-TCPP; the activity of the resultant modified MOF was approximately 7.2 times higher than that of unmodified Zr-TCPP. Fluorination of the carboxylates and a nanosheet morphology further promoted H_2O_2 production by improving the reactivity toward substrates. The hydrophobicity of Zr-TCPP-RF*x* resulting from the modification with perfluorocarboxylates favored the activation of O_2 in an aqueous phase, efficiently suppressed H_2O_2 decomposition, and enhanced the selectivity of the 2-WOR to produce H_2O_2, thus leading to superior activity toward the visible-light-driven photosynthesis of H_2O_2 from O_2 and H_2O. This work provides new insights into MOF photocatalysis and proposes a promising strategy of hydrophobicity control for photocatalytic H_2O_2 production via a two-channel pathway.

Author contributions

The manuscript was written through contributions of all authors. All authors approved the final version of the manuscript. Y. Kondo performed the catalyst preparation, characterization, catalytic reactions, and wrote the manuscript. S. M. performed the catalyst preparation, characterization, catalytic reactions. Y. Kuwahara assisted with N_2 sorption measurements and supervised the project and the experiments. K. M. performed TEM observations and supervised the project and the experiments. T. S. supervised the project and the experiments. H. Y. conceived and supervised the project and the experiments. The manuscript was written through discussion with all authors.

Conflicts of interest

The authors declare no competing financial interest.

Acknowledgements

This work was partially supported by a Grant-in-Aid for Scientific Research (No. 22H00275) and a Grant-in-Aid for Research Activity Start-up (No. 23K19181) from the Japan Society for the Promotion of Science (JSPS). Y. Kondo thanks the JSPS Research Fellowship for Young Scientists (No. 21J10556). Y. Kondo acknowledges financial support from Izumi Science and Technology Foundation. TEM observations were carried out using a facility in the Research Center for Ultra-High Voltage Electron Microscopy, Osaka University. The authors are grateful to Prof. Chiharu Yamanaka for his technical support of the ESR measurements.

Notes and references

1 Y. Kondo, Y. Kuwahara, K. Mori and H. Yamashita, *Chem*, 2022, **8**, 2924–2938.

2 T. Yoshii, Y. Kuwahara, K. Mori and H. Yamashita, *J. Catal.*, 2021, **394**, 259–265.

3 Y. Yamada, M. Yoneda and S. Fukuzumi, *Energy Environ. Sci.*, 2015, **8**, 1698–1701.

4 S. Kato, J. Jung, T. Suenobu and S. Fukuzumi, *Energy Environ. Sci.*, 2013, **6**, 3756–3764.

5 D. Tan, R. Zhuang, R. Chen, M. Ban, W. Feng, F. Xu, X. Chen and Q. Wang, *Adv. Funct. Mater.*, 2024, **34**, 1–24.

6 Y. Zhao, Y. Kondo, Y. Kuwahara, K. Mori and H. Yamashita, *Appl. Catal. B Environ.*, 2024, **351**, 123945.

7 Y. Isaka, Y. Kondo, Y. Kawase, Y. Kuwahara, K. Mori and H. Yamashita, *Chem. Commun.*, 2018, **54**, 9270–9273.

8 Y. Kondo, K. Hino, Y. Kuwahara, K. Mori, H. Kobayashi and H. Yamashita, *Chem. Commun.*, 2022, **58**, 12345–12348.

9 M. Sun, X. Wang, Y. Li, H. Pan, M. Murugananthan, Y. Han, J. Wu, M. Zhang, Y. Zhang and Z. Kang, *ACS Catal.*, 2022, **12**, 2138–2149.

10 Z. Chen, H. Chen, K. Wang, J. Chen, M. Li, Y. Wang, P. Tsiakaras and S. Song, *ACS Catal.*, 2023, **13**, 6497–6508.

11 K. Fuku, R. Takioka, K. Iwamura, M. Todoroki, K. Sayama and N. Ikenaga, *Appl. Catal. B Environ.*, 2020, **272**, 119003.

12 Y. Kondo, K. Honda, Y. Kuwahara, K. Mori, H. Kobayashi and H. Yamashita, *ACS Catal.*, 2022, **12**, 14825–14835.

13 P. Verma, Y. Kondo, Y. Kuwahara, T. Kamegawa, K. Mori, R. Raja and H. Yamashita, *Catal. Rev.*, 2021, **63**, 165–233.

14 Y. Kondo, K. Hino, Y. Kuwahara, K. Mori and H. Yamashita, *J. Mater. Chem. A*, 2023, **11**, 9530–9537.

15 K. Mori, J. Matsuo, Y. Kondo, H. Hata and H. Yamashita, *ACS Appl. Energy Mater.*, 2021, **4**, 11634–11642.

16 Y. Kondo, Y. Kuwahara, K. Mori and H. Yamashita, *J. Phys. Chem. C*, 2021, **125**, 27909–27918.

17 T. He, B. Ni, S. Zhang, Y. Gong, H. Wang, L. Gu, J. Zhuang, W. Hu and X. Wang, *Small*, 2018, **14**, 10–15.

18 F. Drache, V. Bon, I. Senkovska, C. Marschelke, A. Synytska and S. Kaskel, *Inorg. Chem.*, 2016, **55**, 7206–7213.

19 C. Yang, F. Sun, Z. Qu, X. Li, W. Zhou and J. Gao, *ACS Energy Lett.*, 2022, **7**, 4398–4407.

20 Y. Fan, Y. Chen, W. Ge, L. Dong, Y. Qi, C. Lian, X. Zhou, H. Liu, Z. Liu, H. Jiang and C. Li, *J. Am. Chem. Soc.*, 2024, **146**, 7575–7583.

21 S. Wan, C. Dong, J. Jin, J. Li, Q. Zhong, K. Zhang and J. H. Park, *ACS Energy Lett.*, 2022, **7**, 3024–3031.

22 C. Xia, S. Back, S. Ringe, K. Jiang, F. Chen, X. Sun, S. Siahrostami, K. Chan and H. Wang, *Nat. Catal.*, 2020, **3**, 125–134.

23 A. Venugopal, L. H. T. Egberts, J. Meeprasert, E. A. Pidko, B. Dam, T. Burdyny, V. Sinha and W. A. Smith, *ACS Energy Lett.*, 2022, **7**, 1586–1593.

24 H. Hu, Z. Wang, L. Cao, L. Zeng, C. Zhang, W. Lin and C. Wang, *Nat. Chem.*, 2021, **13**, 358–366.

25 P. Deria, J. E. Mondloch, E. Tylianakis, P. Ghosh, W. Bury, R. Q. Snurr, J. T. Hupp and O. K. Farha, *J. Am. Chem. Soc.*, 2013, **135**, 16801–16804.

26 R. Thür, N. Van Velthoven, V. Lemmens, M. Bastin, S. Smolders, D. De Vos and I. F. J. Vankelecom, *ACS Appl. Mater. Interfaces*, 2019, **11**, 44792–44801.

27 R. Li, S. Alomari, R. Stanton, M. C. Wasson, T. Islamoglu, O. K. Farha, T. M. Holsen, S. M. Thagard, D. J. Trivedi and M. Wriedt, *Chem. Mater.*, 2021, **33**, 3276–3285.

28 J. Yang, Z. Wang, K. Hu, Y. Li, J. Feng, J. Shi and J. Gu, *ACS Appl. Mater. Interfaces*, 2015, **7**, 11956–11964.

29 F. Liu, I. Rincón, H. G. Baldoví, A. Dhakshinamoorthy, P. Horcajada, S. Rojas, S. Navalón and A. Fateeva, *Inorg. Chem. Front.*, 2024, **11**, 2212–2245.

30 K. Kise, K. Yoshida, R. Kotani, D. Shimizu and A. Osuka, *Chem. - A Eur. J.*, 2018, **24**, 19136–19140.

31 I. Robayo-Molina, A. F. Molina-Osorio, L. Guinane, S. A. M. Tofail and M. D. Scanlon, *J. Am. Chem. Soc.*, 2021, **143**, 9060–9069.

32 L. Zanetti-Polzi, A. Amadei, R. Djemili, S. Durot, L. Schoepff, V. Heitz, B. Ventura and I. Daidone, *J. Phys. Chem. C*, 2019, **123**, 13094–13103.

33 P. Deria, J. Yu, R. P. Balaraman, J. Mashni and S. N. White, *Chem. Commun.*, 2016, **52**, 13031–13034.

34 J. Nicks, K. Sasitharan, R. R. R. Prasad, D. J. Ashworth and J. A. Foster, *Adv. Funct. Mater.*, 2021, **31**, 2103723.

35 Q. Sun, H. He, W. Y. Gao, B. Aguila, L. Wojtas, Z. Dai, J. Li, Y. S. Chen, F. S. Xiao and S. Ma, *Nat. Commun.*, 2016, **7**, 1–7.

36 W. Zhang, Y. Hu, J. Ge, H. L. Jiang and S. H. Yu, *J. Am. Chem. Soc.*, 2014, **136**, 16978–16981.

37 Y. Shiraishi, M. Jio, K. Yoshida, Y. Nishiyama, S. Ichikawa, S. Tanaka and T. Hirai, *JACS Au*, 2023, **3**, 2237–2246.

38 Y. Nosaka and A. Y. Nosaka, *Chem. Rev.*, 2017, **117**, 11302–11336.

39 J. Luo, Y. Liu, C. Fan, L. Tang, S. Yang, M. Liu, M. Wang, C. Feng, X. Ouyang, L. Wang, L. Xu, J. Wang and M. Yan, *ACS Catal.*, 2021, **11**, 11440–11450.

40 J. Wentworth P., L. H. Jones, A. D. Wentworth, X. Zhu, N. A. Larsen, I. A. Wilson, X. Xu, W. A. Goddard, K. D. Janda, A. Eschenmoser and R. A. Lerner, *Science*, 2001, **293**, 1806–1811.

41 X. Xu, R. P. Muller and W. A. Goddard, *Proc. Natl. Acad. Sci. U. S. A.*, 2002, **99**, 3376–3381.

42 S. Zhao and X. Zhao, *Appl. Catal. B Environ.*, 2019, **250**, 408–418.

43 J. Liu, Y. Zou, B. Jin, K. Zhang and J. H. Park, *ACS Energy Lett.*, 2019, 4, 3018–3027.